iceTEA: Tools for plotting and analysing cosmogenic-nuclide surface-exposure data from former ice margins

R.S. Jones[a,*], D. Small[a], N. Cahill[b], M.J. Bentley[a], P.L. Whitehouse[a]

[a] Department of Geography, Durham University, South Road, Durham, UK
[b] Department of Mathematics and Statistics, Maynooth University, Maynooth, Kildare, Ireland

ABSTRACT

Cosmogenic-nuclide surface-exposure data provide important constraints on the thickness, extent and behaviour of ice masses in the geological past. A number of online calculators provide the cosmogenic nuclide community with a means of easily calculating surface-exposure ages. Here we provide a platform for plotting and analysing such data. This paper describes a suite of freely accessible numerical tools for visualising, evaluating and correcting surface-exposure data that are used to reconstruct past glacier and ice sheet geometries.

iceTEA (Tools for Exposure Ages) is available as an online interface (http://ice-tea.org) and as MATLAB© code. There are 8 tools, which provide the following functionality: 1) calculate exposure ages from ^{10}Be and ^{26}Al data, 2) plot exposure ages as kernel density estimates and as a horizontal or vertical transect, 3) identify and remove outliers within a dataset, 4) plot nuclide concentrations on a two-isotope diagram and as a function of depth, 5) correct exposure ages for cover of the rock surface, 6) correct ages for changes in relative elevation through time, and estimate 7) average and 8) continuous rates of ice margin retreat or thinning. Three of the tools (1, 5 and 6) perform exposure age calculations, which are based on the framework of CRONUScalc. Results are available as printed text, tables and/or raster (.png) and vector (.eps) graphics files, depending on the tool. These tools are intended to enable users to evaluate complex exposure histories, assess the reliability of exposure ages, explore potential age corrections, and better analyse and understand spatial and temporal patterns within their data.

1. Introduction

Over the last few decades cosmogenic-nuclide surface-exposure dating has become the principal approach for reconstructing past glacier and ice sheet geometries (Balco, 2011; Ivy-Ochs and Briner, 2014). Such research has greatly improved our understanding of global and regional patterns of ice mass expansion and contraction (e.g. Hughes et al., 2016; Solomina et al., 2015), centennial-scale climate events (e.g. Schaefer et al., 2009), topographic controls on ice dynamics (e.g. Jones et al., 2015), and contributions of ice masses to past changes in global mean sea level (e.g. Alley et al., 2005). Despite considerable advances in the technique, the full potential of cosmogenic-nuclide datasets is often hindered by geologic scatter, an inadequate assessment of uncertainties and/or limited user expertise in computer coding for performing analyses.

Surface-exposure dating exploits the accumulation of nuclides in the Earth's surface resulting from interactions with cosmic radiation to determine the time at which a rock was exposed following deglaciation

(Gosse and Phillips, 2001). The exposure history can be deciphered from analysis of both the nuclide concentrations and the corresponding surface-exposure ages in a number of ways. The pattern of burial and exposure over glacial-interglacial cycles can be gauged by evaluating the ratio between two different nuclides (e.g. Bierman et al., 1999; Lal, 1991; Schaefer et al., 2016). The reliability of an age for a glacial landform can be assessed with statistical tests such as reduced chi-squared and outlier analysis of the exposure age dataset (e.g. Balco, 2011; Rinterknecht et al., 2006; Wendt and Carl, 1991). Potential effects from cover of the rock surface or changes in the relative elevation of the rock surface can be accounted for and tested (e.g. Cuzzone et al., 2016; Schildgen et al., 2005). Rates of ice surface lowering and ice margin retreat can also be estimated by quantifying the relationship between the location and exposure age of samples within a dataset (e.g. Briner et al., 2009; Johnson et al., 2014). While the development of online exposure age calculators (CRONUS-Earth, Balco et al., 2008; CRONUScalc, Marrero et al., 2016; CREp, Martin et al., 2017) have helped facilitate the rapid growth of the application, there is currently

---

Table 1

Tools of iceTEA.

Tool	MATLAB[©] front-end script	Online stages
1. Calculate ages[a]	Calc_Plot_age.m	Inputs Results Plot Settings Plot Results
2. Plot ages	Import_Plot_age.m	Inputs Plot Results
3. Remove outliers	Calc_Plot_age.m Import_Plot_age.m	Inputs Results Plot Settings Plot Results
4. Plot isotope concentrations	Plot_concs.m	Inputs Plot Results
5. Correct for surface cover[a]	Cover_correct_ages.m	Inputs Results Plot Settings Plot Results
6. Correct for elevation change[a]	Elev_correct_ages.m	Inputs Results Plot Settings Plot Results
7. Estimate retreat/thinning rates - linear approach	Analyse_linear_rates.m	Inputs Results Plot Settings Plot Results
8. Estimate retreat/thinning rates - continuous approach	Analyse_continuous_rates.m	Inputs Results Plot Settings Plot Results

[a] Uses modified version of CRONUScalc calculation framework (Marrero et al., 2016).

no common platform for quantitatively evaluating exposure age data-sets in the ways described above.

Here we describe iceTEA – Tools for Exposure Ages – a suite of online tools for plotting and analysing cosmogenic-nuclide surface-exposure data that are used to constrain former ice margins. The paper outlines the systematics of iceTEA, the basis, set up and user-inputs for each of the tools, and it also highlights potential benefits of applying the tools to surface-exposure datasets.

2. Description of the numerical tools

2.1. Systematics

The tools of iceTEA are outlined in Table 1. They can be used via an online interface (http://ice-tea.org), but are also available as MATLAB[©] code with an easy-to-use front-end script for each tool (see supplementary material). While the online version performs all primary analysis and plotting functionality for each tool, the code provides the user with greater flexibility to apply the tools for specific needs and also includes some additional options (e.g. selecting specific samples within the dataset to be analysed).

Each tool is comprised of two to four stages, which include input parameters, results of the analysis, plot settings and plotted results (Table 1). iceTEA requires the details of the surface-exposure dataset in a Microsoft[©] Excel[©] or comma-separated values spreadsheet, or in a tab-delimited text file. The following information must be included for each sample: sample name; latitude; longitude; elevation; pressure (if known); relative position (if relevant); sample thickness; bulk density; shielding factor; ^{10}Be concentration (mean and uncertainty, if measured); ^{26}Al concentration (mean and uncertainty, if measured); year collected; and for plotting the nuclides on a two-isotope diagram, the sample depth and final mineral weight (see Appendix A1). As with previous age calculators (CRONUScalc, Marrero et al., 2016; CREp, Martin et al., 2017), the nuclide concentrations should be normalised to 07KNSTD for ^{10}Be (Nishiizumi et al., 2007) and KNSTD for ^{26}Al (Nishiizumi, 2004) before being used with iceTEA (see http://hess.ess.

washington.edu/math/docs/al_be_v22/al_be_docs.html for details).

Four tools require exposure ages to be calculated before performing analysis and plotting, while three tools involve the calculation of exposure ages. The details of each of these tools are described in the sections below. In cases where exposure ages are already known (for example, using a different age calculator, perhaps with a local production rate), the mean age, internal and/or external uncertainty and provided production rate scaling model can be used (see Appendix A1). In cases where exposure ages need to be computed, a modified version of the CRONUScalc calculation framework is used (see Marrero et al., 2016 for details).

Cosmogenic-nuclide production is computed for spallation, the dominant production mechanism at the surface, and for muons, which are important at depth (Gosse and Phillips, 2001). Three principal scaling models for production by spallation can be used with iceTEA, which have been shown to best fit production rate calibration data (Borchers et al., 2016): 1) 'Lm', the time-dependent version of Lal (1991), which uses variations in the dipole magnetic field intensity (Nishiizumi et al., 1989); 2) 'LSD', the time-dependent model of Lifton et al. (2014), which includes dipole and non-dipole magnetic field fluctuations and solar modulation; and 3) 'LSDn', a version of LSD that implements nuclide-specific scaling by incorporating cross-sections for the different reactions (Lifton et al., 2014). The MATLAB[©] version of iceTEA has options for other time-independent (St; Stone, 2000) and time-dependent models (De, Du, Li; Desilets and Zreda, 2003; Dunai, 2000; Lifton et al., 2005). The geomagnetic history used in all of the time-dependent scaling models includes the CALS3k model for 0–3 ka (Korte and Constable, 2011; Korte et al., 2009), the CALS7k model for 3–7 ka (Korte and Constable, 2005), the GLOPIS-75 model for 7–18 ka (Laj et al., 2004), and the PADM2M model for 18–2000 ka (Ziegler et al., 2011), which is the same as used in CRONUScalc. Muon flux is scaled using the energy-dependent model of Lifton et al. (2014). All time-dependent scaling models are computed relative to the year that the sample was collected, which is a required input for each sample. As the production rate is dependent on any shielding of the rock surface (Dunne et al., 1999; Gosse and Phillips, 2001), a topographic shielding

factor is a required input for each sample; this can be calculated using the online calculator described by Balco et al. (2008) (http://stoneage. ice-d.org/math/v3/skyline_in.html), or by using the supplemental tool Topographic_shielding.m, which is available in the MATLAB$^©$ version of iceTEA. Nuclide production is numerically integrated for both time, using the selected scaling model, and the depth of the sample, based on the given sample thickness (see Marrero et al., 2016). The implementation of CRONUScalc within iceTEA is further described and discussed in Sections 2.2, 2.6 and 2.7.

2.2. Calculate ages

iceTEA provides the capability to compute and plot surface-exposure ages. The primary purpose of the 'Calculate ages' tool (no. 1) is to compare the calculated ages with those ages generated using correction tools (e.g. correcting for surface cover (Section 2.6) and elevation change (Section 2.7)), as well as to ages derived from other calculation frameworks (e.g. the online calculator formerly known as CRONUS-Earth (Balco et al., 2008), CREp (Martin et al., 2017) and CRONUScalc (Marrero et al., 2016)). While the age calculations in iceTEA are based on the CRONUScalc framework, exposure ages calculated using this tool may produce slightly different results from CRONUScalc for a number of reasons. Firstly, atmospheric pressure is calculated based on the location of each sample if it is not input by the user. The ERA-40 atmospheric model (Uppala et al., 2005) is used to derive pressure, as with CREp and CRONUScalc, however, an elevation-pressure relationship (Radok et al., 1996) is instead used if the sample is from Antarctica (< -60 ˚S) (Balco et al., 2008; Stone, 2000). Secondly, exposures ages are calculated here assuming zero nuclide inheritance, zero surface erosion, and the top depth of a sample is assumed to be the surface (zero depth). Thirdly, the effective attenuation length cannot be manually set, and is instead calculated dependent on the location of the sample (Sato et al., 2008); this is the same method used by CRONUScalc when the attenuation length field is missing. Fourthly, uncertainty is only calculated here based on the elevation and measurement errors, as well as those inherent in the production rate estimates. The exclusion of additional uncertainties (e.g. associated with the bulk density, sample thickness, shielding factor, attenuation length, and erosion rate) reduces computation time relative to CRONUScalc by approximately a factor of four (based on tests using the St and LSD scaling models).

Surface-exposure ages are computed using the provided input data (Section 2.1), and the outputs can then be plotted based on the user's plotting preferences. The age distributions are plotted as kernel density estimates, and age population statistics are calculated if the dataset is defined as being from a single feature (described in Section 2.3). When using the MATLAB$^©$ version, the production rate through time can also be output and plotted.

2.3. Plot ages

The user may wish to plot and evaluate an exposure age dataset that was independently generated using a different calculation program (or previously generated with iceTEA). This tool (no. 2) allows exposure ages to be imported (as specified in Appendix A1) and then plotted.

A useful initial approach for evaluating a population of exposure ages is to look at the age distribution of the dataset. Ages are plotted using this tool as kernel density estimates, which are estimates for the probability density function. Details of this method are discussed in Lowell (1995), however, the version here corrects for the effect in which measurements with the same relative precision have shorter kernel heights – appearing less important – as they get older. The probability distributions are normalised by the expected kernel heights, which are calculated as a function of age, assuming that all measurements have the same relative uncertainty (Balco, 2018). Exposure ages are normally distributed around the mean value, and the type of uncertainty adopted depends on the dataset. External uncertainties

(associated with both the measurement and production rate) are used to calculate the age distributions, unless the dataset is identified as being from a single 'feature' (e.g. a moraine), when the internal uncertainties (measurement only) are instead used; for such datasets, uncertainty introduced due to differences in production rate between samples is typically negligible. Individual age distributions are plotted with the summed age distribution of the dataset.

Exposure ages from a feature should ideally represent a single age population. Statistics describing the age distribution of the dataset are calculated when 'feature' is set by the user. These include the modal age based on the summed age distribution, the weighted mean and standard deviation, and the reduced chi-squared. The weighted mean ($\bar{\mu}$) and weighted standard deviation ($\bar{\sigma}$) of the dataset are calculated as:

$$\bar{\mu} = \sum_i \left(\frac{1/v_i}{\sum_i 1/v_i} \right) x_i \tag{1}$$

and

$$\bar{\sigma} = \sqrt{\sum_i \left(\frac{1/v_i}{\sum_i 1/v_i} \right)(x_i - \bar{\mu})^2} \tag{2}$$

where v_i is a sample's analytical age uncertainty and x_i is a sample's mean age. If preferred, it is possible to alternatively calculate the arithmetic (unweighted) mean and standard deviation (MATLAB$^©$ version only). The reduced chi-squared (χ_R^2) – often referred to as the mean square of the weighted deviations (MSWD) in some areas of geochronology (e.g. Wendt and Carl, 1991) – is a measure of the goodness of fit between the weighted mean and the set of exposure ages. It is calculated as follows:

$$\chi_R^2 = \frac{1}{n-1} \sum_{i=1}^{n} \frac{(x_i - \bar{\mu})^2}{v_i^2} \tag{3}$$

where the degrees of freedom is one less than the number of samples (n). A χ_R^2 value of approximately 1 signifies that the scatter in the dataset can be explained by the measurement uncertainty of the individual samples alone, producing a univariate normal distribution where the weighted mean and uncertainty appropriately represent the data. The measurement uncertainties may have been overestimated if the value is significantly less than 1. For values larger than 1, the observed scatter of the data exceeds that predicted by the age uncertainties, indicating an additional source for variance in the data, most likely from geomorphic factors. To test whether the data represent a single feature, a reduced chi-squared value should fall within a 2σ envelope (95% confidence), determined by the criterion κ:

$$\kappa = 1 + 2\sqrt{\frac{2}{n-1}} \tag{4}$$

which depends on the degrees of freedom and, therefore, the number of samples (Spencer et al., 2017; Wendt and Carl, 1991). If $\chi_R^2 < \kappa$ then there is a > 95% probability that the data represent a single population and it is therefore appropriate to use the weighted mean as an age estimate for the feature (Spencer et al., 2017). A thorough evaluation of a dataset from a single feature should also attempt to identify outliers, which uses different statistical methods (see Section 2.4).

For spatially-variable datasets where samples have been collected at a range of locations relative to an ice margin, it is informative to show exposure ages as a function of their sample position. If the dataset is identified by the user as a 'transect', then exposure ages are additionally plotted as either a vertical or horizontal transect. The relative position is used from the input data (Appendix A1), which should be in metres for a vertical transect and km for a horizontal transect. If there are no relative position values entered for samples from a vertical transect, then the elevation (in metres above sea level) is used.

A series of plotting options are available. The user can set the time axis limits (lower and upper) in thousands of years before present (ka),

and position axis limits (lower and upper) in metres or km depending on the type of relative position data (applies only to the transect plot). In the MATLAB$^©$ version, particular samples within the dataset can be selected to plot (the default is to plot all samples given in the input data).

2.4. Remove outliers

Glacial chronologies often have a degree of scatter where samples do not provide matching exposure ages. For glacial features, such as moraines or bedrock landforms, a suite of samples is typically collected to provide an accurate age constraint. While the shape of a summed probability distribution can be used to indicate potential outliers – a single discrete peak implies all ages with uncertainties are consistent with each other, more than one discrete peak implies no single consistent age population, and a peak with a shoulder peak on one of its limbs implies something in between – it is partially subjective. To more robustly identify whether a dataset represents a single age population or a dominant age population and an outlier, statistical outlier tests like the Chauvenet's criterion (e.g. Rinterknecht et al., 2006) and Grubbs' Test (e.g. Putnam et al., 2010), and assessments of dataset skewness (Applegate et al., 2010) have been applied.

In this tool (no. 3) we use a two-tailed generalised extreme Studentized deviate (gESD) test to statistically identify whether there are any outliers within the dataset (Rosner, 1983). Similar to the Grubbs' Test (Grubbs, 1969), it assumes that the data can be approximated by a normal distribution, and is performed iteratively using the difference between the sample's mean exposure age and the most extreme data considering the standard deviation. Unlike the Grubbs' Test, the gESD test does not assume a single outlier, and instead uses an upper bound for the number of possible outliers (r). The outliers are calculated from a sequence of separate tests (1 outlier, 2 outliers, ..., r outliers):

$$R_i = \frac{|x^{(i)} - \bar{x}^{(i)}|}{s^{(i)}} \tag{5}$$

where R_i is Rosner's test statistic representing the extreme Studentized deviates from successively reduced samples, $x^{(i)}$ is the observation with the greatest distance from the mean of the dataset, and $\bar{x}^{(i)}$ and $s^{(i)}$ are the mean and standard deviation of the dataset with the most extreme observations removed. Critical values (λ_i) for R_i are calculated as:

$$\lambda_i = \frac{t_{p,n-i-1}(n-i)}{\sqrt{(n-i-1+t_{p,n-i-1})(n-i+1)}} \tag{6}$$

where n is the number of observations, t_p is the Student's t-distribution for the quantile of significance level α (the default is 0.05; 5% probability of incorrectly rejecting the null hypothesis that there are no outliers), and $n - i - 1$ determines the degrees of freedom.

The number of outliers is determined by finding the iteration with the most successively reduced samples (the largest i). If $R_i > \lambda_i$ then the i most extreme values are outliers. We set the maximum number of outliers (r) as $n - 1$; by assuming a high number of possible outliers, we avoid additional outliers influencing the value of the test statistic. The method is most accurate for datasets with at least 15 samples, and particularly > 25 samples (Rosner, 1983). Datasets with fewer samples require there to be much fewer outliers for accurate detection. For example, at the most extreme, no more than a single outlier could be reliably identified from a dataset of only 3 samples.

The outlier identification and removal tool is featured differently in the online and MATLAB$^©$ versions of iceTEA. The tool is included within the age calculation and plotting tools (Sections 2.2 and 2.3) in the MATLAB$^©$ version (Table 1). On the web interface it is a separate tool, requiring sample exposure ages to be calculated and included in the input sample data (Appendix A1). By using the tool, it is assumed that the data come from a single feature (e.g. a moraine or bedrock

landform), and that there should be a consistent age population for that feature. If a dataset contains multiple features, then the analysis must be performed separately for each feature, with the input data organised accordingly. For a more thorough assessment of a dataset, the significance level for determining outliers (α) can be optionally set to 0.01 (default is 0.05), which would instead generate results with a 1% probability of incorrectly rejecting the null hypothesis that there are no outliers. Once the outliers have been identified and removed, the reduced dataset of the feature is plotted as a kernel density plot with the corresponding modal age, weighted mean and standard deviation, and reduced chi-squared statistic (as in Section 2.3). The removed outliers can optionally be plotted as grey kernel density estimates. If no outliers are detected then this plot will contain all original ages within the dataset. The user can optionally set the time axis limits (lower and upper) of the plot in thousands of years before present (ka), and specify which samples to plot (MATLAB$^©$ version only).

2.5. Plot isotope concentrations

Multiple nuclides (most commonly ^{10}Be and ^{26}Al) are often measured in a sample to better understand the exposure and burial history (Lal, 1991), and can be particularly useful in burial dating and for identifying cosmogenic inheritance in a sample (e.g. Fabel and Harbor, 1999; Granger, 2006). The 'Plot isotope concentrations' tool (no. 4) enables measured nuclide concentrations to be plotted on a two-isotope diagram and optionally as a depth profile, using the information provided in the input data. It should be noted that the required data are slightly different from that needed for the other tools (see Section 2.1 and Appendix A1). The tool is currently only available for ^{10}Be and ^{26}Al data.

The purpose of a two-isotope diagram is to compare measured nuclide concentrations with those concentrations that should be expected from simple pathways of exposure and burial (Fig. 1). The concentration of a nuclide (N_k) during exposure differs between isotopes, owing to nuclide-specific production and decay:

$$N_k = \frac{P_k}{\lambda_k + \frac{\rho\varepsilon}{\Lambda}}\left(1 - exp\left[-\left(\lambda_k + \frac{\rho\varepsilon}{\Lambda}\right)\right]t_e\right) \tag{7}$$

where P_k is the nuclide's production rate (atoms g^{-1} a^{-1}), λ_k is the nuclide's decay constant (a), ρ is rock density (g cm^{-3}), ε is the surface erosion rate (cm a^{-1}), Λ is the attenuation length (g cm^{-2}), and t_e is the exposure time (a). For a continuously exposed rock surface, the concentration of ^{10}Be increases until it reaches secular equilibrium, while the ratio of ^{26}Al to ^{10}Be decreases as the lower half-life of ^{26}Al causes it reach secular equilibrium sooner (top curve in Fig. 1). A rock surface can experience different concentration pathways despite continuous exposure as a result of subaerial erosion. A second, lower curve is determined by calculating nuclide saturation from continuous exposure and a multitude of erosion rates. A steady-state erosion island (Lal, 1991) – referred to here as the "simple exposure region" – represents the area within which a continuously exposed surface can exist (Fig. 1). Following exposure, when a surface becomes buried and protected from cosmic rays, the concentration of ^{26}Al decays more quickly than that of ^{10}Be; the ^{26}Al/^{10}Be ratio decreases in line with radioactive decay. Exposure and burial isochrones, representing concentrations of equal exposure (t_e) and burial (t_b) time (a), are plotted on the diagram and calculated with:

$$N_k = \frac{P_k}{\lambda_k + \frac{\rho}{\Lambda}}\left(1 - exp\left[-\left(\lambda_k + \frac{\rho}{\Lambda}\right)\right]t_e\right)exp\left[-\left(\lambda_k + \frac{\rho}{\Lambda}\right)\right]t_b \tag{8}$$

where it is assumed that the surface is buried at an infinite depth, with zero production, following initial continuous exposure rather than steady-state erosion. The diagram (Fig. 1) assumes that a sample has primarily experienced spallogenic production, at or near to the surface, rather than muonic production at greater depths. In situations where a
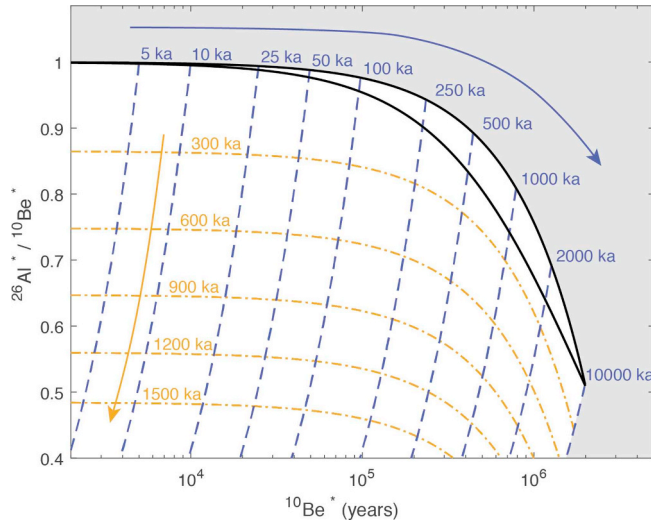
Fig. 1. A two-isotope diagram for normalised ^{10}Be and ^{26}Al concentrations. During continuous exposure, the ^{10}Be concentration increases until it becomes saturated and is at secular equilibrium (upper black line). Meanwhile, the ^{26}Al/^{10}Be ratio decreases. Surfaces that are continuously exposed but that undergo different degrees of constant erosion follow diverging trajectories until saturation is reached (lower black line). Any rock surfaces with measured concentrations that fall between these lines – the simple exposure region – are assumed to have been continuously exposed with a "simple" exposure history. Concentrations that plot above these lines (in the grey area) are either not feasible and imply issues with the geochemistry or measurement of a sample, imply that a sample was once exposed at a higher elevation (larger production rate) and then transported to a lower elevation, or indicate that a sample underwent production for a substantially long period at depth (larger ^{26}Al/^{10}Be production ratio) before arriving at the surface. Concentrations that plot below the simple exposure region indicate that the sampled surface has been buried with a "complex" exposure history. Isochrones highlight points of equal exposure time (purple dashed lines) and burial time (orange dot-dashed lines).

sample underwent significantly more production at depth (i.e. below ~5 m) than at the surface – for fast-eroding settings and/or deep cores – the ratio between ^{26}Al and ^{10}Be would be greater (e.g. Akçar et al., 2017; Granger and Smith, 2000) and the sample would appear further up the diagram (Fig. 1).

To allow for comparing samples from multiple sites, it is necessary to normalise nuclide concentrations. A depth-integrated local present-day production rate of each sample is calculated and averaged by the mineral weight, while the mean density and attenuation length of the samples are used to compute the exposure and burial isochrones and lines of continuous exposure. As the nuclide concentrations are normalised by the nuclide's production rate, P_k in Equations (7) and (8) becomes equal to 1.

The plot can also be produced for nuclide concentrations from core samples, where some samples may have been combined for a nuclide measurement. An example is where, at a particular depth range, two samples were independently measured for ^{10}Be but were combined for ^{26}Al measurement (e.g. Schaefer et al., 2016). Based on the sample input data (see Section 2.1 and Appendix A1), data are automatically sorted by finding common depths between nuclide measurements and then combining the normalised concentration means ($\hat{N}_c$) and uncertainties ($\widehat{\sigma N_c}$) for the depth range:

$$\hat{N}_c = \frac{\sum_c (\hat{N}_s \sum w_s)}{\sum_c (\sum w_s)}$$

(9)

and

$$\widehat{\sigma N_c} = \sqrt{\left(\frac{\sum_c (\hat{N}_s \sum w_s)}{\sum_c (\sum w_s)}\right)^2}$$

(10)

where $\hat{N}_s$ is the normalised sample concentration (with the unit being years, as the concentration is normalised by the production rate) and w_s is the weight of each sample (g).

The two-isotope diagram uses a logarithmic axis for the normalised ^{10}Be concentration (Nishiizumi et al., 1991) as 1) it reduces clustering of samples, particularly for low ^{10}Be concentrations, and 2) radioactive decay lines and corresponding burial isochrones are near-straight, allowing for simpler interpretation of data with respect to time. Sample concentrations are plotted with uncertainty ellipses and a point mean. The ellipses can be shown for either 1 or 2 σ (68% or 95% confidence). The user can also optionally set the ^{26}Al/^{10}Be ratio and ^{10}Be concentration axes limits (lower and upper) and, in the MATLAB© version, set the exposure and burial isochrones (in ka) to plot.

Depth profiles can be particularly useful for evaluating nuclide production in soils and bedrock (e.g. Balco and Rovey, 2008; Schaefer et al., 2016). This tool provides the option to additionally plot sample concentrations (in atoms g^{-1}) as a function of depth (m), where a box represents the depth range and the concentration uncertainty of each sample, and a line represents the mean concentration for that sample. The depth and concentration axes limits (lower and upper) can be optionally set when producing this plot using the MATLAB© version.

2.6. Correct for surface cover

Cosmogenic nuclide production in rock decreases with depth below the surface as cosmic radiation is attenuated. The same process occurs in material overlying the rock surface – dependent on the thickness and density of that material – which can shield the rock surface from cosmic rays and therefore reduce nuclide production (Gosse and Phillips, 2001). The effects of shielding from surface cover are commonly ignored or considered negligible, but feasible depths of $> 16\,\mathrm{g\,cm^{-2}}$ reduce nuclide production by $> 10\%$. Two main approaches can be taken if a study region is suspected to have had some surface cover (e.g. snowpack, soil, loess, till, ash, water): 1) a specific sampling strategy to minimise the effects of possible surface cover – for example, only the top surfaces of large boulders could be sampled, assuming that these would not have been covered or that any material was quickly wind-swept (e.g. Balco, 2011; Ivy-Ochs et al., 1999); or 2) the influence of surface cover on collected rock samples could be evaluated by calculating surface cover shielding factors and resulting exposure ages (e.g. Benson et al., 2004; Schildgen et al., 2005).

Here we provide a tool (no. 5) that calculates exposure ages with a correction for material covering the rock surface. The total time-averaged surface shielding factor (S_S) is calculated from:

$$S_S = S_T \exp\left(-\frac{z_{cover}\, \rho_{cover}}{\Lambda_s}\right)$$

(11)

where S_T is the shielding factor from topography (Dunne et al., 1999), and where shielding from surface cover is determined from the average depth of surface cover (z_{cover}, in cm), the average density of that cover (ρ_{cover}, in g cm^{-3}) and the effective attenuation length (Λ_s, in g cm^{-2}). The topographic shielding factor is taken from the sample input data (see Section 2.1), while the attenuation length is determined from the sample location (see Section 2.2). A value for cover depth is required, as well as either a preset cover type (Table 2) or a manually specified density for the surface cover. Exposure ages are then calculated as described in Marrero et al. (2016) and Section 2.2.

The cover shielding factor computed in this tool is a simplified approach to be used to test the effects from long-term averages of surface cover, as it assumes that surface cover was of constant depth for the entire period of interest. In reality, snow cover at a site likely varied through time with seasonal fluctuations, water levels could have varied

Table 2
Preset cover material options and the corresponding density (ρ_{cover}) used for surface cover corrections. A user-specified density for surface cover can alternatively be used.

Cover material	Density (g cm^{-3})
Ash	0.7
Loess	1.6
Snow	0.27
Soil	1.3[a]
Till	1.8
Fresh water	0.999[b]
Sea water	1.027[c]

[a] Average of dry mineral soil ($\sim$1–1.6 g cm^{-3}); note, a value for wet soil will be higher.

[b] Near-surface water (1.1 bars) at 10 °C.

[c] Near-surface water (1.1 bars) at 10 °C with salinity of 35 g kg^{-1}.

periodically or lowered progressively, and till, soil, loess and ash-type deposits may have gradually deflated over time. In locations where snow cover was likely prevalent, there are methods available that use seasonal changes in snow-depth (Gosse and Phillips, 2001), or an energy balance model to account for temporal and spatial variability of snow shielding (Schildgen et al., 2005). Ideally, corrected exposure ages should use a time-dependent shielding factor, however this requires estimates of the cover depth (and density) through time, which is rarely possible to approximate. It should also be noted that a more complex mass-shielding approach is possibly required to accurately account for production from thermal neutron capture (Delunel et al., 2014; Dunai et al., 2014; Zweck et al., 2013) and for variations in cover density with depth (Jonas et al., 2009).

Results are provided following computation of the shielding factor and corresponding exposure ages for the specified production scaling method. These results include the surface cover and total shielding factors, and the corrected surface-exposure ages (mean and standard deviation). The corrected age distributions are plotted as kernel density estimates (described in Section 2.3).

2.7. Correct for elevation change

Cosmogenic nuclide production is dependent on atmospheric pressure, with greater production occurring at higher altitudes where the pressure is lower (Gosse and Phillips, 2001; Lal, 1991). An accurate estimate of the atmospheric pressure during exposure is, therefore, necessary for the calculation of an exposure age. Typically, it is assumed that the elevation of a sampled surface relative to sea level – the reference point for scaling atmospheric pressure – has either not varied over time or that any effect of elevation change is negligible. However, while atmospheric pressure at present-day sea level was likely similar to today in the past (Mélières et al., 1991), we know from models of glacial isostatic adjustment (GIA) (e.g. Peltier et al., 2015) that vertical deformation of the land varied over time in response to changing volumes of ice masses. Where a surface-exposure dating site is located next to the coast, a relative sea-level curve has previously been used to estimate relative changes in elevation since ice retreated from that region (e.g. Goehring et al., 2012; Rinterknecht et al., 2006; Young et al., 2013). Away from the coast and relative sea-level sites, it is not possible to accurately extrapolate any recorded elevation changes, largely because the local ice loading history and resulting glacial isostatic response vary in space (cf. Whitehouse, 2018). In such cases, GIA models can be used to derive exposure ages that are corrected for isostatic change (e.g. Cuzzone et al., 2016; Suganuma et al., 2014; Ullman et al., 2016). Tectonically-driven elevation change will also have an effect on nuclide production (Dunai, 2010; Riihimaki and Libarkin, 2007). Rock samples that have been exposed over long timescales, or that are from

areas of rapid uplift/subsidence, may therefore also require correction of local production rates and resulting exposure ages (e.g. Brook et al., 1995; Dunai et al., 2005; Schaefer et al., 1999).

In this tool (no. 6), exposure ages are calculated with corrections for changes in elevation – derived from either a GIA model or a linear rate (uplift or subsidence) – through time. The time-varying (t) elevation relative to sea level (E) is determined from:

$$E_m(t) = e_{pres,m} + e_{diff,m}(t) \tag{12}$$

where $e_{pres,m}$ is the present-day elevation (m asl) of a sample (m), and $e_{diff,m}(t)$ is the elevation (metres) of a sample relative to $e_{pres,m}$ at time t. For a given rate (m ka^{-1}), $e_{diff,m}(t)$ is computed back to 8160 ka before present (approx. 6 times the half-life of ^{10}Be) in 100-year intervals. Using a GIA-derived correction, $e_{diff,m}(t)$ is the past isostatic elevation change, interpolated from model output at 100-year intervals. $E_m(t)$ is then converted to atmospheric pressure, dependent on its location (see Section 2.2). The total nuclide production is calculated based on the corrected atmospheric pressure (p):

$$P_{total,k}(t) = S_{el,\zeta}(p, R_c, t) S_S \, P_{ref,s,\zeta,k} \, exp\left(\frac{-z}{\Lambda_s}\right) + S_S P_\mu(p, R_c, z) \tag{13}$$

where $S_{el,\zeta}$ is the time-dependent elevation-latitude scaling factor for a particular scaling model (ζ), S_S is the shielding factor from terrain and surface cover (see Section 2.6), $P_{ref,s,\zeta}$ is the reference spallogenic (s) production rate (atom g^{-1} a^{-1}) at present-day sea-level high-latitude (where $p = 1013.25$) for nuclide k, Λ_s is the effective attenuation length (g cm^{-2}), z is the depth (g cm^{-2}), and P_μ is the production rate (atom g^{-1} a^{-1}) at z due to muons (μ), which is a function of pressure, depth and the cutoff rigidity (R_c). Applying a GIA-based correction to the primary ^{10}Be calibration sites of Borchers et al. (2016) increases the time- and site-averaged production rate by just 0.17% (based on the ICE-6G ice model and LSD scaling model), well within the uncertainty of the measurements and calculation (Jones et al., in review). The reason for only a minor correction is largely because the sites were far enough away from the centres of past major glacial isostatic change. For long-term subsidence or uplift, it can be assumed that effects were region-specific and did not influence production at the calibration sites. We therefore use the uncorrected spallogenic production rate of Borchers et al. (2016) for calculating exposure ages that are corrected for changes in relative elevation.

Determination of the time-dependent relative elevation of a sample ($e_{diff,m}(t)$) requires particular inputs based on whether the GIA model or linear rate approach is used. For the linear rate method, a rate of elevation change (m ka^{-1}) is required to generate an elevation history. A positive rate (e.g. 2 m ka^{-1}) would correspond to lower elevations in the past, uplifting towards present, and a negative rate would correspond to higher elevations in the past, subsiding towards present. For the GIA-based method, either the ICE-5G (Peltier, 2004) or ICE-6G (Peltier et al., 2015) ice model can be selected, which are the only global ice models currently freely available. Most ice masses are included in these models (Antarctica, Greenland, Laurentide, Cordilleran, Fennoscandian, British-Irish, Patagonian, New Zealand, and Iceland), but the relatively minor effects from ice in the Himalayas, European Alps, Caucasus and Andes do not feature. There are some differences between the ice models, particularly in North America, but ICE-6G is considered to be more accurate as it is constrained by modern GPS-measured uplift rates in addition to ice extent and relative sea-level records. The original ice model data was also produced for different timescales, with ICE-5G ice history defined from 122 ka to present, but ICE-6G from just 26 ka. Prior to these times, the elevation difference for the oldest model time step is used and, therefore, corrected exposure ages older than 122 ka or 26 ka should not be interpreted.

In addition to defining the ice-load history, the rheological properties of the Earth must be prescribed within the GIA model. A three-layer approximation of the VM2 Earth model (5G reference) is used in our calculations. The VM2 Earth model was developed in conjunction

with the ICE-5G ice model, while the ICE-6G ice model was developed in parallel with the VM5a Earth model (6G reference). VM5a is simply a multi-layer fit to VM2, so our 3-layer approximation is appropriate for use with both ice models. Having defined both the ice model and the Earth model, the time-dependent elevation relative to present can be calculated. The spatial resolution of the GIA model output used within iceTEA is 1 geographic degree, meaning that a greater spatial variability of isostatic effects is captured towards the poles. The GIA model accounts for shoreline migration, rotational feedbacks, and the gravitational attraction of ice masses (Milne and Mitrovica, 1998; Whitehouse, 2018). If the sample elevation is below sea level for any particular period of time, then it is assumed that no nuclide production occurs.

Results are provided following computation of the time-dependent elevation and corresponding exposure ages for the specified production scaling method. These results include the corrected surface-exposure ages (mean and standard deviation) and the mean offsets from the uncorrected ages (in years and as a percentage), which are exported as an Excel© spreadsheet or text file. The corrected age distributions are plotted as kernel density estimates (described in Section 2.3), and the local production rates used are plotted as a function of time. The age axes of the plots, as well as the production rate axis, can be optionally set (lower limit and upper limit).

2.8. Estimate retreat/thinning rate – linear approach

Surface-exposure dating is sometimes applied in transects to constrain spatial changes of the ice margin through time (e.g. Briner et al., 2009; Cuzzone et al., 2016; Johnson et al., 2014; Lane et al., 2014; Small et al., 2018). Linear rates of deglaciation can then be estimated by either calculating the distance and age offset between dated positions, or by performing regression analysis for a suite of exposure ages that vary approximately linearly with their position. The latter approach has been used to derive average rates and corresponding durations of rapid ice surface lowering in Antarctica (Johnson et al., 2014; Jones et al., 2015; Small et al., 2019), and is adopted here (tool no. 7).

Ice margin retreat or thinning rate estimates are computed for datasets that form either a horizontal or vertical transect, respectively. The positions of the samples relative to the ice margin (in km for horizontal transects and metres for vertical transects) are used as the independent variable in the analysis. Least-squares regression is applied randomly to normally-distributed exposure ages (at 2 σ) through a Monte Carlo simulation; while 5000 is the default number of iterations, this value can be optionally specified. Linear least-squares regression predicts the exposure age (y_i) for each sample position regressor (q_i):

$$y_i = \beta_0 + \beta_1 q_i \tag{14}$$

where β_1 is the Pearson correlation coefficient of the observed mean exposure ages and sample positions, multiplied by the standard deviation of the mean ages divided by the standard deviation of the positions, and β_0 is the mean of the observed ages minus the mean of the observed sample positions multiplied by β_1.

The approach assumes that 1) the exposure ages accurately represent the timing of ice margin retreat or ice surface lowering at each position, without any post-depositional processes or cosmogenic inheritance significantly affecting the ages, and 2) retreat/thinning was approximately continuous over the time period. Rates are estimated from the distribution of feasible, positive-sloping linear regressions. The uncertainty of the estimate is generally reflective of the number and scatter of exposures ages contributing to each transect, together with their respective uncertainties. Uncertainties in the horizontal/vertical positions of samples are not included in the calculations.

Linear estimates can be computed using either unweighted or weighted regression, where the weighting is derived from the analytical uncertainty of each sample (see Equations (1) and (2)). While the weighted method should be used if some of the exposure ages have large uncertainties relative to others in the dataset, the unweighted method should be used if outliers within the data are suspected, particularly if those potential outliers have relatively small uncertainties.

The computed linear rates are produced as a probability distribution, with estimates at 68% and 95% confidence bounds. Estimated rates are plotted as a histogram, highlighting the modal and median rate, and as a transect, showing all modelled linear regressions for the exposure ages as a function of sample position. For the latter plot, the user can specify whether to show the exposure ages, and can optionally set the time and relative position axes (lower and upper limits) in thousands of years before present and in metres or km, respectively. In the MATLAB© version, the samples to be analysed within the dataset can also be specified (the default is to analyse all samples).

2.9. Estimate retreat/thinning rates – continuous approach

A surface-exposure dataset may record a variable rate of ice retreat or thinning during deglaciation (e.g. Lane et al., 2014; Spector et al., 2017). In this case an average rate derived from a linear regression model (Section 2.8) will not adequately capture the ice margin or ice surface elevation changes implied by the data. Alternatively, the continuous evolution of such changes can be modelled to derive rate estimates, enabling the magnitude and timing of rate changes to be identified and datasets from different locations to be compared (e.g. Cahill et al., 2015).

Here we provide a tool (no. 8) that estimates rates of retreat or thinning by fitting a continuous time-dependent function of ice position with respect to time. The relative position (distance from ice margin or elevation above the modern ice surface) is modelled using Fourier Series analysis:

$$f(t) = a_0 + \sum_{i=1}^{n} a_i \cos(wti) + b_i \sin(wti) \tag{15}$$

where $f(t)$ is the true relative sample position under the assumptions of the fitted model, t is the mean age of the mean sample position, a_i and b_i are coefficients for the cosine and sine forms, w is the frequency of the signal, and i is the number of terms in the series. The latter of these parameters can be optionally modified to manually improve the fit of the model to the data (values are accepted between 1 and 8; default is 3); the higher the number of terms (i), the more sinusoidal the fit. While potentially useful, this is a simple approach that 1) uses only the mean exposure age and position values, 2) may assume that the exposure ages can record retreat/thinning and advance/thickening, and 3) requires the user to decide which model (determined by the number of terms) best fits the data.

The MATLAB© version of iceTEA includes an additional, more robust statistical approach, designed for surface-exposure data. In this case, the relative position is modelled using Bayesian penalized spline regression:

$$f(t_i) = \sum_{k=1}^{K} b_k(t)\alpha_k \tag{16}$$

where t_i is the age of the sample position and $f(t_i)$ is the true relative position under the assumptions of the fitted model, α_k refers to spline coefficient k and b_k is the kth B-spline evaluated at age t, for $k = 1, ...,K$. Cubic B-splines (e.g. Eilers and Marx, 2010) were used and the first order differences of the spline coefficients were penalized to ensure smoothness of the fitted curve. As surface-exposure dating assumes continuous deglaciation without readvance or re-thickening, a further constraint was imposed on the coefficients so that the spline-modelled positions decreased over time. The model was fitted within a Bayesian framework using JAGS (just another Gibbs sampler; Plummer, 2003) to provide estimates of $f(t_i)$ with uncertainties, which were incorporated through an errors-in-variables framework (Cahill et al., 2015; Dey et al.,

2000). For a vertical transect, both temporal (exposure age) and spatial (elevation) uncertainties are included, while just the exposure age uncertainty is used for a horizontal transect.

Computed time-dependent estimates are produced for the median, and 68% and 95% confidence bounds. The fitted age-position profile is plotted together with the rates of change as a function of time, and the minimum and maximum median rates are identified and highlighted. The user can specify whether to show the exposure ages, and can optionally set the time, relative position and rate of change axes (lower and upper limits) in thousands of years before present, in metres or km, and in cm yr^{-1} or m yr^{-1}, respectively. In the MATLAB$^©$ version, the samples to be analysed within the dataset can be specified (the default is to analyse all samples), and the number of Monte Carlo iterations within the Bayesian framework can be set (the default is 20,000).

3. Example applications and outputs

The iceTEA tools can be used for most ^{10}Be and ^{26}Al surface-exposure datasets that are used to constrain former ice margins, but the choice of tool depends on the context of the dataset. Each of the tools plot nuclide concentrations, exposure ages, and/or results of an analysis, which are available for download using the online interface or can be automatically saved using the MATLAB$^©$ code, in both raster-based Portable Network Graphics (.png) and vector-based Encapsulated Postscript (.eps) formats. This section highlights potential applications for each of the tools and provides overviews for the graphical outputs of iceTEA.

The duration and nature of past ice cover can be apparent from nuclide concentrations alone, without the need for calculating corresponding exposure ages. Rock samples that have paired ^{10}Be and ^{26}Al measurements can be evaluated with the 'Plot isotope concentrations' tool (no. 4) (Fig. 2). Measured nuclide concentrations that plot within the simple exposure region likely record continuous exposure since first exposed, while concentrations that plot below this area indicate that the sample underwent at least one period of burial since first exposed. In Fig. 2A, the measured concentrations from a Greenland bedrock core (Schaefer et al., 2016) – corresponding to core segments at 0.22–0.99 m and 1.02–1.29 m (Fig. 2B) – imply at least ~25–50 ka of exposure and ~700–1600 ka of burial. Such applications can help reveal the relative duration of past ice cover and whether the landscape was covered by cold-based, non-erosive ice (e.g. Briner et al., 2006), but can also be combined with numerical modelling approaches to identify potential glacial/interglacial scenarios (e.g. Schaefer et al., 2016).
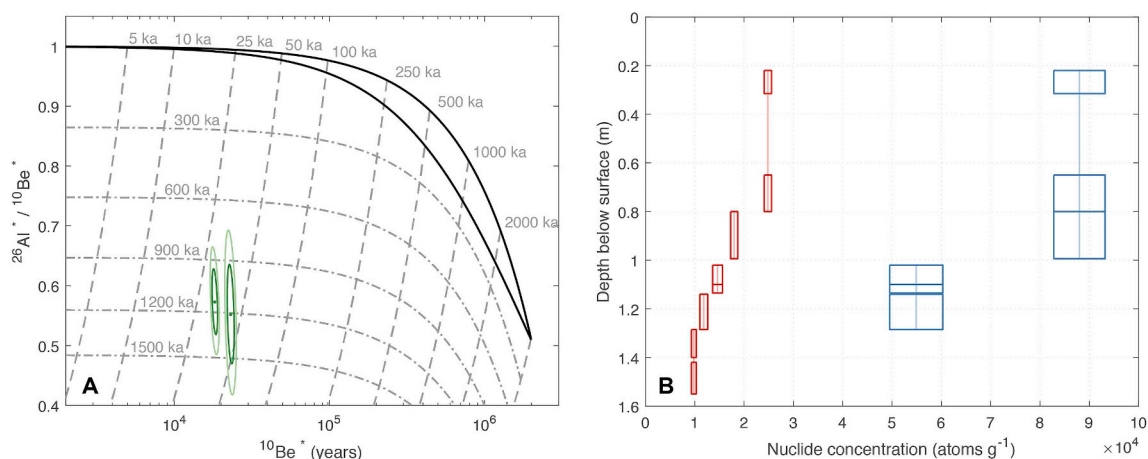
Most of the plotting and analysis tools are for use with surface-exposure ages. The overall distribution of ages within a dataset can be visualised with a kernel density plot, using either the 'Calculate ages' or 'Plot ages' tool (no. 1 and 2, respectively). For a geographically-distributed dataset (e.g. sequence of moraines, isolated bedrock features or glacial deposits), temporal patterns in the chronology such as those across a region of New Zealand can be identified (Fig. 3A). It should be noted, however, that such an application would have to assume that none of the exposure ages were biased by post-depositional disturbance or inheritance of nuclides from prior exposure, making an apparent age younger or older respectively. For datasets from a vertical or horizontal transect, patterns of ice surface lowering or ice margin retreat can be interpreted from a plot of the relative positions against exposure ages (Fig. 3B).

The 'Remove outliers' tool (no. 3) is for diagnosing exposure ages within a dataset derived from a single glacial feature. In an example from a moraine in southern Patagonia (Fig. 4A), 14 exposure ages produce a consistent mean and modal age for the feature. However, the spread of ages within the dataset result in a large reduced chi-squared value that is greater than the chi-squared criterion, therefore implying that the mean and standard deviation should not be used to represent the age population (at 95% confidence). Applied to this example, four exposure ages are identified as outliers and are removed from the dataset (Fig. 4B). This results in a much tighter cluster of ages and a decreased reduced chi-squared that is indicative of a single age population (at 95% confidence). Based on both the reduced chi-squared test and gESD outliers test, a weighted mean and standard deviation of 14.22 ± 0.5 ka can be used as the age for this moraine. Ideally, a reason for an outlier should be established whenever one or more are identified – for example, evidence that the sample has experienced surface erosion or post-depositional movement. Outlier removal approaches rely on the assumption that geomorphic processes do not influence each sample equally. If such effects did occur equally – for example, potentially from surface erosion if the samples are of the same lithology and approximately the same age – then the mean ages would shift but the scatter of ages within the dataset would not be significant.

Two of the iceTEA tools (no. 7 and 8) estimate rates of deglaciation from a transect of exposure ages. Average rates of retreat or thinning can be computed using the linear model (no. 7) (Fig. 5). This approach is best applied when the position-age relationship of a dataset implies an approximately constant rate of retreat or thinning. In cases where all ages within a transect have overlapping uncertainties, instantaneous retreat or thinning is feasible, but the median and range of rates from
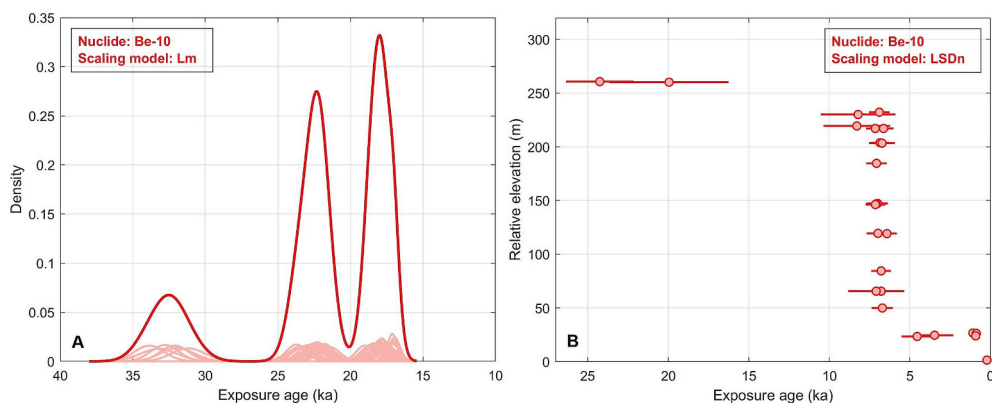

Fig. 2. Nuclide concentrations plotted A) on a two-isotope diagram (at 1 and 2 sigma), and B) as a function of depth (at 1 sigma). These are examples produced by the tool 'Plot isotope concentrations', which reproduce previously published plots of ^{10}Be (red) and ^{26}Al (blue) nuclide concentrations that were measured in a bedrock core (Schaefer et al., 2016). In this case, those core segments that were combined for nuclide measurement are automatically detected based on common sample depths (linked with a vertical line through the means in B) in order to produce the equivalent ^{10}Be and ^{26}Al nuclide concentrations that are shown in A. It is unlikely that samples would be combined for surface rock samples, and therefore each sample would be plotted on the two-isotope diagram separately.

Fig. 3. Exposure ages plotted as A) kernel density estimates for samples from a sequence of moraines (Ohau II-VI, Lake Ohau, New Zealand; Putnam et al., 2013), and B) a vertical transect recording ice sheet surface lowering (Mt Suess and Low Ridge, Mackay Glacier, Antarctica; Jones et al., 2015). These are examples of the plotted outputs from the tools 'Calculate ages' and 'Plot ages', which are able to highlight temporal and spatial patterns within datasets.
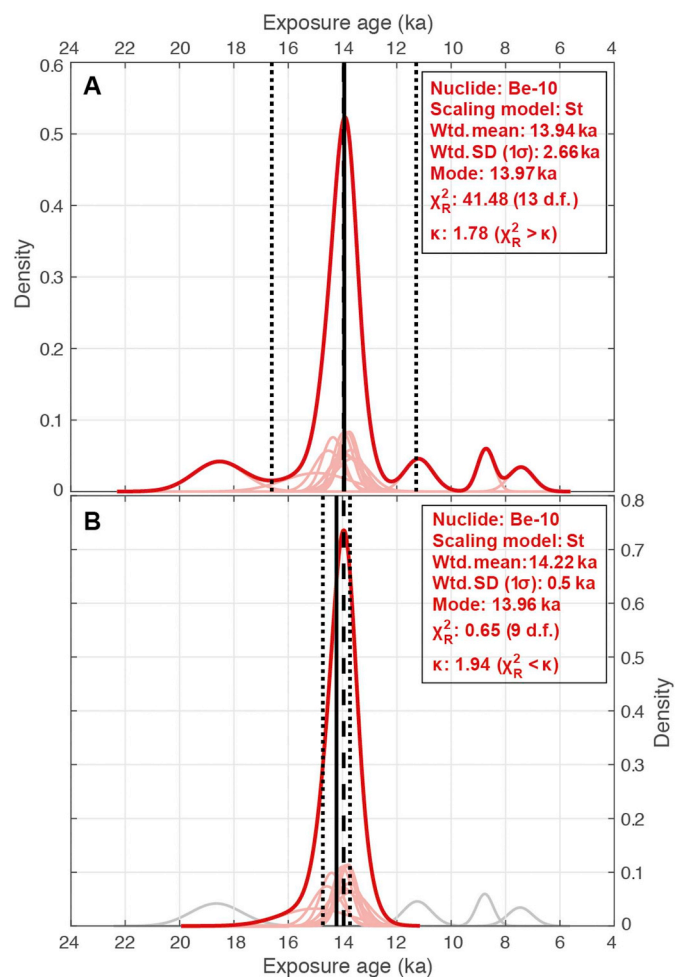

Fig. 4. Exposure ages from a moraine plotted as kernel density estimates A) for the initial raw dataset, and B) following the removal of outliers. The example dataset is from Torres del Paine, southern Patagonia (TDPIII, n = 14; García et al., 2012). Using the 'Calculate ages' or 'Plot ages' tool, the probability distribution of each sample is plotted in light red and the summed distribution of the dataset is plotted as a bold red line. Additionally, the mode (black dashed line), weighted mean (black solid line) and weighted standard deviation (SD; black dotted lines) of the dataset are shown, and the reduced chi-squared (χ^2_R) and associated criterion (κ) are calculated; if $\chi^2_R < \kappa$ then there is a > 95% probability that the data represent a single population (d.f. is degrees of freedom). Four outliers were identified (plotted in grey) and removed in this example using a generalised extreme Studentized deviate (gESD) test with the 'Remove outliers' tool.

the regression analysis provide a more probable estimate based on the age uncertainties (Fig. 5D). Transects of exposure ages that imply a variable rate (e.g. periods of both gradual and rapid retreat/thinning) are less suited to this tool, and should instead be used with the Fourier or spline based models (tool no. 8) to compute continuous rates. In Fig. 6, modelled surface lowering profiles are plotted for a vertical transect, as well as the corresponding rates of thinning for the period covered by the dataset, for both model approaches. The quality of the fit may vary between approaches, dependent on dataset. In this example, the Fourier Series analysis (number of terms = 3) indicates that the minimum rate of ice surface lowering was equal to or less than 0 cm yr^{-1} at multiple times, with a maximum median lowering rate of 14.7 cm yr^{-1} at 7.3 ka. Using the spline-based approach provides an improved fit, indicating that ice surface lowering was slowest at 10.7 ka, but then accelerated to a maximum median rate of 15.1 cm yr^{-1} at 8.1 ka before becoming more gradual after ~6 ka. Irrespective of the approach used to estimate deglaciation rates, the effects from potential outliers within a dataset should be investigated.

Two iceTEA tools (no. 5 and 6) perform age corrections for a dataset. The 'Correct for surface cover' tool (no. 5) can be used for testing the sensitivity of an exposure age dataset if past cover of rock surfaces is suspected. Fig. 7 highlights that the shielding provided by surface cover causes the resulting exposure ages to become older. This effect is greater for a higher density cover material, such as till relative to snow, and for thicker cover, for example 50 cm relative to 20 cm (Fig. 7). While this approach is useful for examining the effects of shielding by surface cover, the true exposure ages will always be uncertain unless the cover depth and density are confidently known for the full exposure history.

The 'Correct for elevation change' tool (no. 6) can be used to understand the potential exposure age effects from either a long-term approximately constant rate of tectonic rock uplift/subsidence or GIA changes over the last glacial-interglacial cycle. Tectonic impacts will unsurprisingly be largest at sites near to a plate boundary, such as in the Himalaya. Effects from GIA are both spatially and temporally variable (Jones et al., in review). Broadly, corrected exposure ages will become older if they are derived from a region of significant deglaciation (e.g. Norway in Fig. 8) due to glacial isostatic depression at the time of initial exposure, can become younger if located at an isostatically elevated, subsiding 'peripheral bulge' region beyond an ice sheet margin (e.g. north-eastern USA in Fig. 8), or could be relatively unchanged if they are from a region of negligible surface elevation change (e.g. England in Fig. 8). The period during which samples have been exposed will also have an effect – for example, a sample that becomes exposed early in the deglaciation (e.g. at 20 ka) will have potentially experienced greater isostatic elevation change than samples initially exposed in the Holocene. While applying these corrections should provide more accurate exposure ages – particularly for regions with large elevation changes – these ages are dependent on the GIA model, including
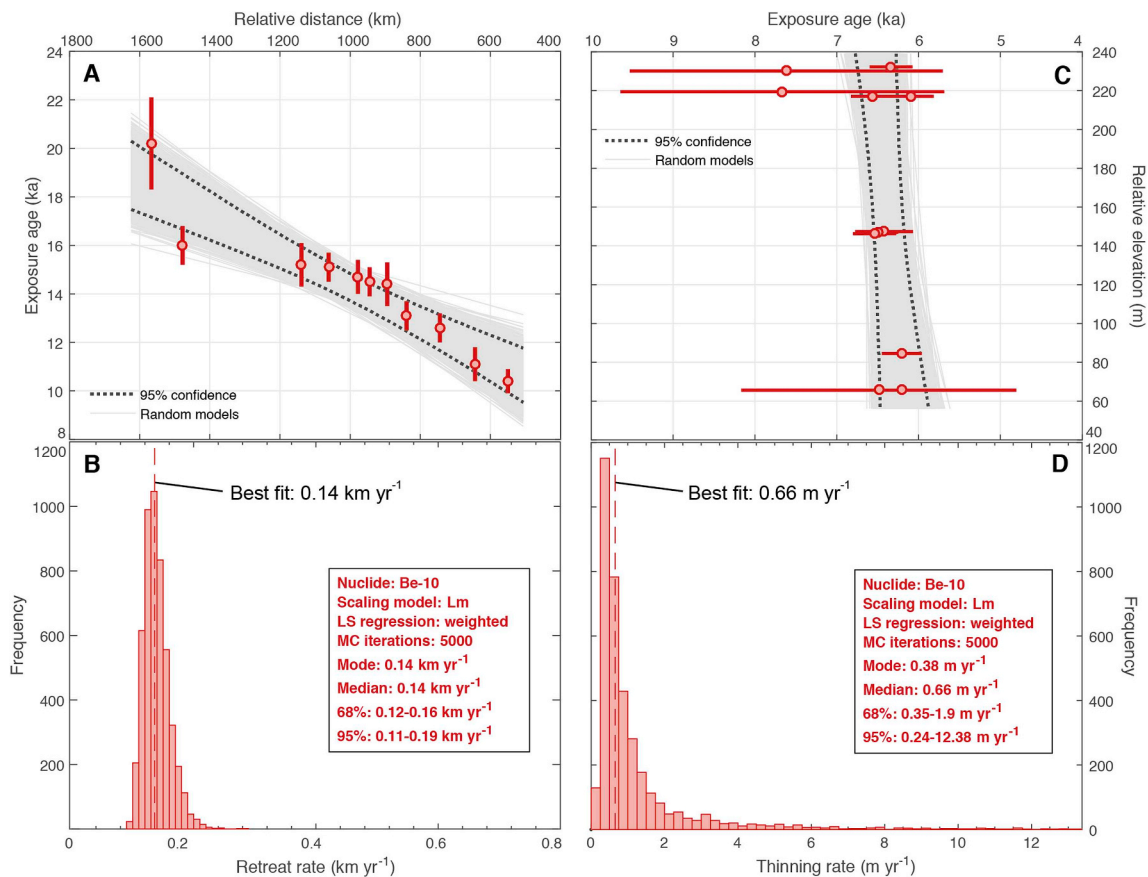
Fig. 5. Example outputs from estimating average deglaciation rates using the linear model. A) The individual linear regressions (grey lines) and the 95% confidence bounds (dashed black lines) are shown for a Monte Carlo (MC) least-squares (LS) linear regression analysis on a horizontal transect of exposure ages. The example data is from the 'Sweden' transect of Cuzzone et al. (2016) and references therein (using the weighted mean ages from individual sites). B) A histogram showing the corresponding distribution of retreat rates produced by each iteration of the linear regression analysis. C) and D) are the same as A and B, but for a vertical transect of exposure ages from Mackay Glacier, Antarctica (Jones et al., 2015).
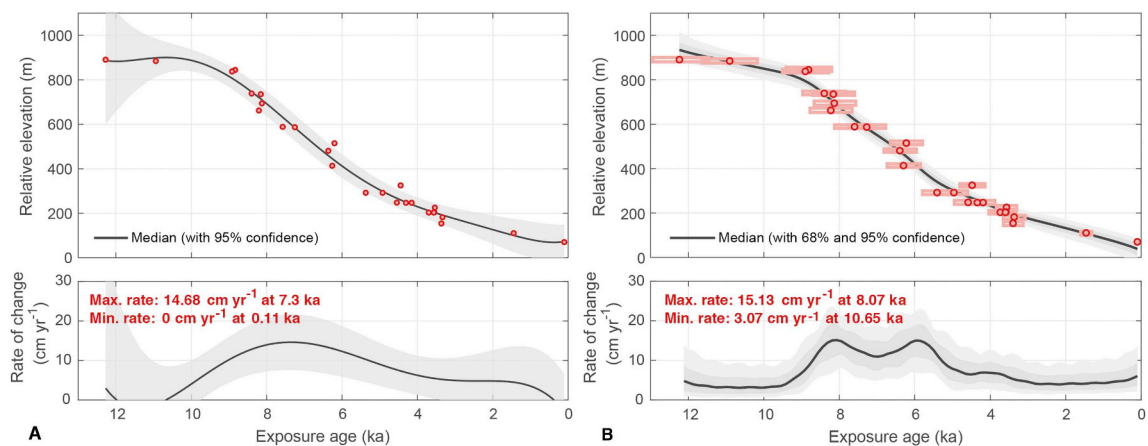
Fig. 6. Example output from estimating continuous deglaciation rates using the A) Fourier and B) spline models. The upper panel is the modelled profile for an example vertical transect (Scott and Reedy Glaciers, Antarctica; Spector et al., 2017). The mean exposure ages are also plotted, with rectangles representing the age and elevation uncertainties used in the spline-based regression. The lower panel is the corresponding rate of change. Maximum and minimum rates, and their respective timings, are also computed.

uncertainties associated with both the quantification of ice sheet change and Earth rheology, or linear estimate of elevation change. At any particular location, the reliability of the correction also depends on

the degree of past atmospheric pressure change in that region (Staiger et al., 2007). This tool will be improved in the future as these effects are better understood and quantified.
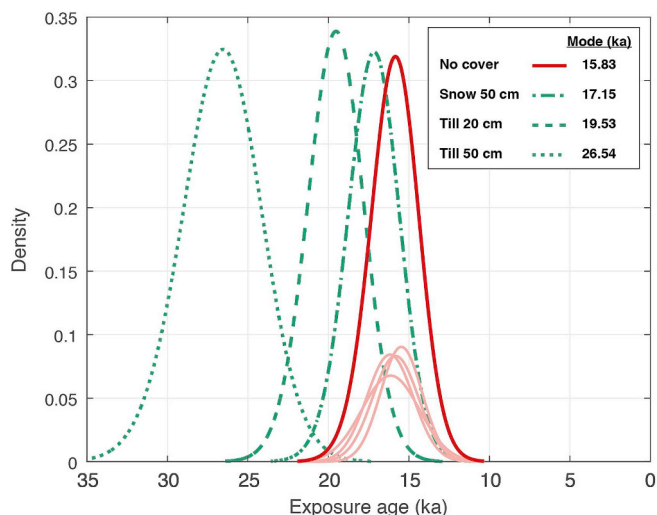
Fig. 7. Effects on exposure ages from example scenarios of material covering sampled rock surfaces. The raw, uncorrected exposure ages are shown as kernel density estimates in light red with the summed density estimate of the dataset as a dark red line. The green curves represent the summed density estimates for varying degrees of shielding by overlying materials (individual age distributions are not shown for clarity), calculated using the 'Correct for surface cover' tool. The dot-dashed curve is cover by 50 cm of snow (assumed density of $0.27\,g\,cm^{-3}$), the dashed curve is cover by 20 cm of till (assumed density of $1.8\,g\,cm^{-3}$), and dotted curve is cover by 50 cm of till. The greater the thickness and density of cover material, the larger the age correction.

4. Conclusions

iceTEA is an online and MATLAB$^{©}$ based suite of tools for plotting and analysing cosmogenic-nuclide surface-exposure data from former glacier and ice sheet margins. The tools allow complex exposure histories to be evaluated using a two-isotope diagram, patterns within exposure age datasets to be identified from kernel density estimate and transect plots, the reliability of exposure ages to be examined with reduced chi-squared and outlier removal tests, linear and continuous rates of retreat or thinning to be estimated, and effects from cover of rock surfaces and time-varying changes in relative elevation to be investigated and corrected ages to be calculated. This paper is not intended to be prescriptive in the approaches taken to analysing exposure ages. Our aim is that these tools will allow workers to explore the spatial and temporal patterns in their data in a consistent and inter-comparable way, and also to initiate discussion of further improvements in the application and analysis of surface-exposure data.

There is also potential for future iceTEA development. Currently these tools can only be used for ^{10}Be and ^{26}Al concentrations and exposure ages, but we intend to expand the code so that it can be used with ^{3}He, ^{14}C, ^{21}Ne and ^{36}Cl data. The age calculation framework will also be updated following any important revisions of the existing geomagnetic databases, production rates and scaling models. It is also hoped that production rates which have been corrected for both time-varying relative elevation and atmospheric pressure changes will be included in the future. We welcome suggestions for additional plotting or analysis tools.
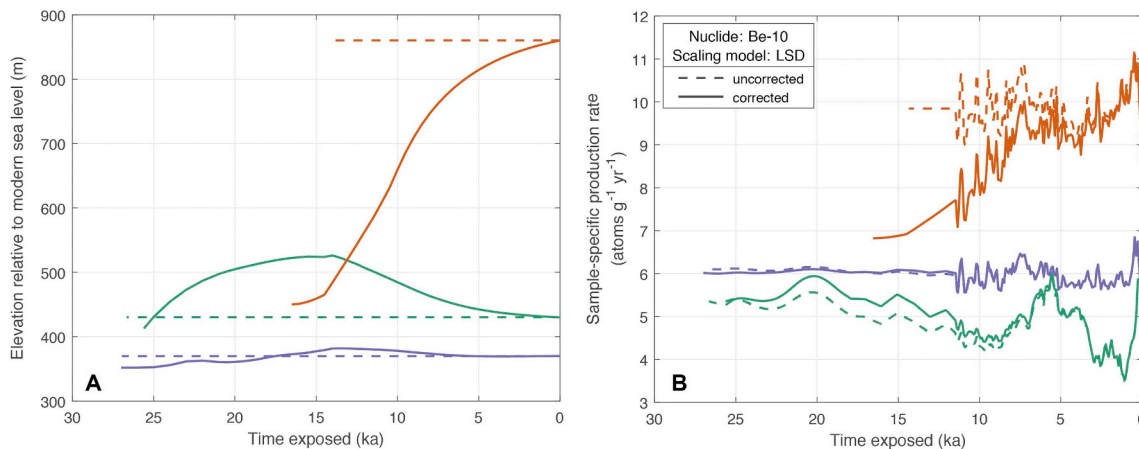
Fig. 8. Effects from GIA. A) The elevation of a sample site relative to present since first exposed, and B) the corresponding change in the site-specific production rate through time. The dashed line assumes no change in GIA, while the solid line is corrected for GIA effects. The orange site is in a region of substantial glacial isostatic uplift (central Norway), the green site was previously isostatically elevated at a 'peripheral bulge' (north-eastern USA), and the purple site is from a region of minor past surface elevation change (central England). The examples were generated using the ICE-6G ice model and LSD nuclide scaling model. The high-frequency production rate variability during the last ~12 ka is from changes in the solar output; the scaling model uses an average value prior to this time as any variability is undefined (Lifton et al., 2014).

Appendix A1. Required sample input data

There are two forms of input data required, which can be in a Microsoft© Excel© (.xlsx) or comma-separated values (.csv) spreadsheet, or in a tab-delimited text file (.txt) without column headings. The standard type of input data is used for all plotting and analysis tools apart from 'Plot isotope concentrations', with 15 required columns plus an optional 7 columns (22 in total) for importing previously calculated exposure ages. For the 'Plot isotope concentrations' tool, 17 columns of sample data are required. Templates called 'input_data_template.xlsx' and 'input_data_template_complex.xlsx' for the two input types, respectively, can be found in the supplementary data, within the compiled MATLAB© code and on the iceTEA website. Templates for example datasets are also available. It is possible with the 'Plot isotope concentrations' tool to sort and plot bedrock core data where some sections may have been combined for nuclide measurement. In such cases, data should be entered with each row representing a separate nuclide measurement (see 'GISP2_input_complex.xlsx').

Appendix A2. Overview of the iceTEA online interface

The home page of iceTEA features links to each of the individual tool interfaces (Figure A1), while a 'Documentation' page provides information on iceTEA, including the MATLAB© code and descriptions of the necessary input data formats. On selecting the desired tool, the user will be taken to an interface (e.g. Figure A2). This will include a series of stages specific to each tool (Table 1), including Inputs, Results, Plot Settings and Plot Results. The user can advance through the stages by selecting 'Next', and will be warned if necessary information is missing. In the initial data input stage, sample data in a correctly formatted input file (Appendix A1) should be uploaded and the tool parameters should be specified. Any results (e.g. calculated ages, corrections, retreat/thinning rate estimates) will be displayed in the Results stage. Plots will be shown in the final stage, which can be downloaded as both raster-based .png and vector-based .eps files.

Fig. A1. Home page of iceTEA, which features links to each of the tool interfaces.

Fig. A2. An example tool interface. The user can progress through each of the stages (e.g. Inputs to Results to Plot Settings to Plot Results), using the 'Next' button.2

Appendix B. Supplementary data

Supplementary data to this article can be found online at https://doi.org/10.1016/j.quageo.2019.01.001.

References

Akçar, N., Ivy-Ochs, S., Alfimov, V., Schlunegger, F., Claude, A., Reber, R., Christl, M., Vockenhuber, C., Dehnert, A., Rahn, M., 2017. Isochron-burial dating of glaciofluvial deposits: first results from the Swiss Alps. Earth Surf. Process. Landforms 42, 2414–2425.

Alley, R.B., Clark, P.U., Huybrechts, P., Joughin, I., 2005. Ice-sheet and sea-level changes. Science 310, 456–460.

Applegate, P., Urban, N., Laabs, B., Keller, K., Alley, R., 2010. Modeling the statistical distributions of cosmogenic exposure dates from moraines. Geosci. Model Dev. (GMD) 3, 293–307.

Balco, G., 2011. Contributions and unrealized potential contributions of cosmogenic-nuclide exposure dating to glacier chronology, 1990–2010. Quat. Sci. Rev. 30, 3–27.

Balco, G., 2018. The "Fancy-pants" Camelplot, the Bleeding Edge of Cosmogenic-Nuclide Geochemistry.

Balco, G., Rovey, C.W., 2008. An isochron method for cosmogenic-nuclide dating of buried soils and sediments. Am. J. Sci. 308, 1083–1114.

Balco, G., Stone, J.O., Lifton, N.A., Dunai, T.J., 2008. A complete and easily accessible means of calculating surface exposure ages or erosion rates from ^{10}Be and ^{26}Al measurements. Quat. Geochronol. 3, 174–195.

Benson, L., Madole, R., Phillips, W., Landis, G., Thomas, T., Kubik, P., 2004. The probable importance of snow and sediment shielding on cosmogenic ages of north-central Colorado Pinedale and pre-Pinedale moraines. Quat. Sci. Rev. 23, 193–206.

Bierman, P.R., Marsella, K.A., Patterson, C., Davis, P.T., Caffee, M., 1999. Mid-Pleistocene cosmogenic minimum-age limits for pre-Wisconsinan glacial surfaces in southwestern Minnesota and southern Baffin Island: a multiple nuclide approach. Geomorphology 27, 25–39.

Borchers, B., Marrero, S., Balco, G., Caffee, M., Goehring, B., Lifton, N., Nishiizumi, K., Phillips, F., Schaefer, J., Stone, J., 2016. Geological calibration of spallation production rates in the CRONUS-Earth project. Quat. Geochronol. 31, 188–198.

Briner, J.P., Bini, A.C., Anderson, R.S., 2009. Rapid early Holocene retreat of a Laurentide outlet glacier through an Arctic fjord. Nat. Geosci. 2, 496.

Briner, J.P., Miller, G.H., Davis, P.T., Finkel, R.C., 2006. Cosmogenic radionuclides from fjord landscapes support differential erosion by overriding ice sheets. Geol. Soc. Am. Bull. 118, 406–420.

Brook, E.J., Brown, E.T., Kurz, M.D., Ackert Jr., R.P., Raisbeck, G.M., Yiou, F.o., 1995. Constraints on age, erosion, and uplift of Neogene glacial deposits in the Transantarctic Mountains determined from in situ cosmogenic ^{10}Be and ^{26}Al. Geology 23, 1063–1066.

Cahill, N., Kemp, A.C., Horton, B.P., Parnell, A.C., 2015. Modeling sea-level change using errors-in-variables integrated Gaussian processes. Ann. Appl. Stat. 9, 547–571.

Cuzzone, J.K., Clark, P.U., Carlson, A.E., Ullman, D.J., Rinterknecht, V.R., Milne, G.A., Lunkka, J.-P., Wohlfarth, B., Marcott, S.A., Caffee, M., 2016. Final deglaciation of the Scandinavian Ice Sheet and implications for the Holocene global sea-level budget. Earth Planet. Sci. Lett. 448, 34–41.

Delunel, R., Bourlès, D.L., van der Beek, P.A., Schlunegger, F., Leya, I., Masarik, J., Paquet, E., 2014. Snow shielding factors for cosmogenic nuclide dating inferred from long-term neutron detector monitoring. Quat. Geochronol. 24, 16–26.

Desilets, D., Zreda, M., 2003. Spatial and temporal distribution of secondary cosmic-ray nucleon intensities and applications to in situ cosmogenic dating. Earth Planet. Sci. Lett. 206, 21–42.

Dey, D.K., Ghosh, S.K., Mallick, B.K., 2000. Generalized Linear Models: A Bayesian Perspective. CRC Press.

Dunai, T., Binnie, S., Hein, A., Paling, S., 2014. The effects of a hydrogen-rich ground cover on cosmogenic thermal neutrons: implications for exposure dating. Quat. Geochronol. 22, 183–191.

Dunai, T.J., 2000. Scaling factors for production rates of in situ produced cosmogenic nuclides: a critical reevaluation. Earth Planet. Sci. Lett. 176, 157–169.

Dunai, T.J., 2010. Cosmogenic Nuclides: Principles, Concepts and Applications in the Earth Surface Sciences. Cambridge University Press.

Dunai, T.J., López, G.A.G., Juez-Larré, J., 2005. Oligocene–Miocene age of aridity in the Atacama Desert revealed by exposure dating of erosion-sensitive landforms. Geology 33, 321–324.

Dunne, J., Elmore, D., Muzikar, P., 1999. Scaling factors for the rates of production of cosmogenic nuclides for geometric shielding and attenuation at depth on sloped surfaces. Geomorphology 27, 3–11.

Eilers, P.H., Marx, B.D., 2010. Splines, knots, and penalties. Wiley Interdisciplinary Reviews: Comput. Stat. 2, 637–653.

Fabel, D., Harbor, J., 1999. The use of in-situ produced cosmogenic radionuclides in glaciology and glacial geomorphology. Ann. Glaciol. 28, 103–110.

García, J.L., Kaplan, M.R., Hall, B.L., Schaefer, J.M., Vega, R.M., Schwartz, R., Finkel, R., 2012. Glacier expansion in southern Patagonia throughout the Antarctic cold reversal. Geology 40, 859–862.

Goehring, B.M., Lohne, Ø.S., Mangerud, J., Svendsen, J.I., Gyllencreutz, R., Schaefer, J., Finkel, R., 2012. Late glacial and Holocene ^{10}Be production rates for western Norway. J. Quat. Sci. 27, 89–96.

Gosse, J.C., Phillips, F.M., 2001. Terrestrial in situ cosmogenic nuclides: theory and application. Quat. Sci. Rev. 20, 1475–1560.

Granger, D.E., 2006. A review of burial dating methods using ^{26}Al and ^{10}Be. In: Siame, L.L., Bourlès, D.L., Brown, E.T. (Eds.), In Situ-Produced Cosmogenic Nuclides and Quantification of Geological Processes. Geological Society of America Special Paper, pp. 1–16.

Granger, D.E., Smith, A.L., 2000. Dating buried sediments using radioactive decay and muogenic production of ^{26}Al and ^{10}Be. Nucl. Instrum. Methods Phys. Res. Sect. B Beam Interact. Mater. Atoms 172, 822–826.

Grubbs, F.E., 1969. Procedures for detecting outlying observations in samples. Technometrics 11, 1–21.

Hughes, A.L., Gyllencreutz, R., Lohne, Ø.S., Mangerud, J., Svendsen, J.I., 2016. The last Eurasian ice sheets–a chronological database and time-slice reconstruction. DATED-1. Boreas 45, 1–45.

Ivy-Ochs, S., Briner, J.P., 2014. Dating disappearing ice with cosmogenic nuclides. Elements 10, 351–356.

Ivy-Ochs, S., Schlüchter, C., Kubik, P.W., Denton, G.H., 1999. Moraine exposure dates imply synchronous younger dryas glacier advances in the European Alps and in the southern Alps of New Zealand. Geogr. Ann. Ser. A Phys. Geogr. 81, 313–323.

Johnson, J.S., Bentley, M.J., Smith, J.A., Finkel, R., Rood, D., Gohl, K., Balco, G., Larter, R.D., Schaefer, J., 2014. Rapid thinning of pine island glacier in the early holocene. Science 343, 999–1001.

Jonas, T., Marty, C., Magnusson, J., 2009. Estimating the snow water equivalent from snow depth measurements in the Swiss Alps. J. Hydrol. 378, 161–167.

Jones, R.S., Mackintosh, A., Norton, K.P., Golledge, N.R., Fogwill, C., Kubík, P.W., Christl, M., Greenwood, S.L., 2015. Rapid Holocene thinning of an East Antarctic outlet glacier driven by marine ice sheet instability. Nat. Commun. 6, 8910.

Jones, R.S., Whitehouse, P.L., Bentley, M.J., Small, D.P., Dalton, A.S., 2019;al., in review. Impact of glacial isostatic adjustment on cosmogenic surface-exposure dating. in review. Quat. Sci. Rev.

Korte, M., Constable, C., 2011. Improving geomagnetic field reconstructions for 0–3ka. Phys. Earth Planet. In. 188, 247–259.

Korte, M., Constable, C.G., 2005. The geomagnetic dipole moment over the last 7000 years—new results from a global model. Earth Planet. Sci. Lett. 236, 348–358.

Korte, M., Donadini, F., Constable, C., 2009. Geomagnetic field for 0–3 ka: 2. A new series of time-varying global models. Geochem. Geophys. Geosyst. 10.

Laj, C., Kissel, C., Beer, J., 2004. High resolution global paleointensity stack since 75 kyr (GLOPIS-75) calibrated to absolute values. Timescales of the Paleomagnetic Field 255–265.

Lal, D., 1991. Cosmic ray labeling of erosion surfaces: in situ nuclide production rates and erosion models. Earth Planet. Sci. Lett. 104, 424–439.

Lane, T.P., Roberts, D.H., Rea, B.R., Cofaigh, C.Ó., Vieli, A., Rodés, A., 2014. Controls upon the last glacial maximum deglaciation of the northern Uummannaq ice stream system, west Greenland. Quat. Sci. Rev. 92, 324–344.

Lifton, N., Sato, T., Dunai, T.J., 2014. Scaling in situ cosmogenic nuclide production rates using analytical approximations to atmospheric cosmic-ray fluxes. Earth Planet. Sci. Lett. 386, 149–160.

Lifton, N.A., Bieber, J.W., Clem, J.M., Duldig, M.L., Evenson, P., Humble, J.E., Pyle, R., 2005. Addressing solar modulation and long-term uncertainties in scaling secondary cosmic rays for in situ cosmogenic nuclide applications. Earth Planet. Sci. Lett. 239, 140–161.

Lowell, T.V., 1995. The application of radiocarbon age estimates to the dating of glacial sequences: an example from the Miami sublobe, Ohio, USA. Quat. Sci. Rev. 14, 85–99.

Marrero, S.M., Phillips, F.M., Borchers, B., Lifton, N., Aumer, R., Balco, G., 2016. Cosmogenic nuclide systematics and the CRONUScalc program. Quat. Geochronol. 31, 160–187.

Martin, L., Blard, P.-H., Balco, G., Lavé, J., Delunel, R., Lifton, N., Laurent, V., 2017. The CREp program and the ICE-D production rate calibration database: a fully parameterizable and updated online tool to compute cosmic-ray exposure ages. Quat. Geochronol. 38, 25–49.

Mélières, M.-A., Martinerie, P., Raynaud, D., Lliboutry, L., 1991. Glacial-interglacial mean sea level pressure change due to sea level, ice sheet and atmospheric mass changes. Glob. Planet. Chang. 3, 333–340.

Milne, G,A., Mitrovica, J.,X., 1998. Postglacial sea-level change on a rotating Earth. Geophys. J. Int. 133, 1–19.

Nishiizumi, K., 2004. Preparation of 26 Al AMS standards. Nucl. Instrum. Methods Phys. Res. Sect. B Beam Interact. Mater. Atoms 223, 388–392.

Nishiizumi, K., Imamura, M., Caffee, M.W., Southon, J.R., Finkel, R.C., McAninch, J., 2007. Absolute calibration of ^{10}Be AMS standards. Nucl. Instrum. Methods Phys. Res. Sect. B Beam Interact. Mater. Atoms 258, 403–413.

Nishiizumi, K., Kohl, C., Arnold, J., Klein, J., Fink, D., Middleton, R., 1991. Cosmic ray produced ^{10}Be and ^{26}Al in Antarctic rocks: exposure and erosion history. Earth Planet. Sci. Lett. 104, 440–454.

Nishiizumi, K., Winterer, E., Kohl, C., Klein, J., Middleton, R., Lal, D., Arnold, J., 1989. Cosmic ray production rates of ^{10}Be and ^{26}Al in quartz from glacially polished rocks. J. Geophys. Res.: Solid Earth 94, 17907–17915 1978–2012.

Peltier, W.R., 2004. Global glacial isostasy and the surface of the ice-age Earth: the ICE-5G (VM2) model and GRACE. Annu. Rev. Earth Planet Sci. 32, 111–149.

Peltier, W.R., Argus, D.F., Drummond, R., 2015. Space geodesy constrains ice age terminal deglaciation: the global ICE-6G_C (VM5a) model. J. Geophys. Res.: Solid Earth 120, 450–487.

Plummer, M., 2003. JAGS: a program for analysis of Bayesian graphical models using Gibbs sampling. In: Proceedings of the 3rd International Workshop on Distributed Statistical Computing. Vienna, Austria.

Putnam, A.E., Denton, G.H., Schaefer, J.M., Barrell, D.J., Andersen, B.G., Finkel, R.C., Schwartz, R., Doughty, A.M., Kaplan, M.R., Schlüchter, C., 2010. Glacier advance in southern middle-latitudes during the antarctic cold reversal. Nat. Geosci. 3, 700.

Putnam, A.E., Schaefer, J.M., Denton, G.H., Barrell, D.J., Birkel, S.D., Andersen, B.G., Kaplan, M.R., Finkel, R.C., Schwartz, R., Doughty, A.M., 2013. The last glacial maximum at 44° S documented by a ^{10}Be moraine chronology at Lake Ohau, Southern Alps of New Zealand. Quat. Sci. Rev. 62, 114–141.

Radok, U., Allison, I., Wendler, G., 1996. Atmospheric surface pressure over the interior of Antarctica. Antarct. Sci. 8, 209–217.

Riihimaki, C.A., Libarkin, J.C., 2007. Terrestrial cosmogenic nuclides as paleoaltimetric proxies. Rev. Mineral. Geochem. 66, 269–278.

Rinterknecht, V., Clark, P., Raisbeck, G., Yiou, F., Bitinas, A., Brook, E., Marks, L., Zelčs, V., Lunkka, J.-P., Pavlovskaya, I., 2006. The last deglaciation of the southeastern sector of the Scandinavian Ice Sheet. Science 311, 1449–1452.

Rosner, B., 1983. Percentage points for a generalized ESD many-outlier procedure. Technometrics 25, 165–172.

Sato, T., Yasuda, H., Niita, K., Endo, A., Sihver, L., 2008. Development of PARMA: PHITS-based analytical radiation model in the atmosphere. Radiat. Res. 170, 244–259.

Schaefer, J.M., Denton, G.H., Kaplan, M., Putnam, A., Finkel, R.C., Barrell, D.J., Andersen, B.G., Schwartz, R., Mackintosh, A., Chinn, T., 2009. High-frequency Holocene glacier fluctuations in New Zealand differ from the northern signature. Science 324, 622–625.

Schaefer, J.M., Finkel, R.C., Balco, G., Alley, R.B., Caffee, M.W., Briner, J.P., Young, N.E., Gow, A.J., Schwartz, R., 2016. Greenland was nearly ice-free for extended periods during the Pleistocene. Nature 540, 252–255.

Schaefer, J.M., Ivy-Ochs, S., Wieler, R., Leya, I., Baur, H., Denton, G.H., Schlüchter, C., 1999. Cosmogenic noble gas studies in the oldest landscape on earth: surface exposure ages of the Dry Valleys, Antarctica. Earth Planet. Sci. Lett. 167, 215–226.

Schildgen, T.F., Phillips, W.M., Purves, R.S., 2005. Simulation of snow shielding corrections for cosmogenic nuclide surface exposure studies. Geomorphology 64, 67–85.

Small, D., Smedley, R.K., Chiverrell, R.C., Scourse, J.D., Ó Cofaigh, C., Duller, G.A., McCarron, S., Burke, M.J., Evans, D.J., Fabel, D., 2018. Trough geometry was a greater influence than climate-ocean forcing in regulating retreat of the marine-based Irish-Sea Ice Stream. Geological Society of America Bulletin.

Small, D., Bentley, M.J., Jones, R.S., Pittard, M.L., Whitehouse, P.L., 2019. Antarctic ice sheet palaeo-thinning rates from vertical transects of cosmogenic exposure ages. Quat. Sci. Rev. 206, 65–80.

Solomina, O.N., Bradley, R.S., Hodgson, D.A., Ivy-Ochs, S., Jomelli, V., Mackintosh, A.N., Nesje, A., Owen, L.A., Wanner, H., Wiles, G.C., 2015. Holocene glacier fluctuations. Quat. Sci. Rev. 111, 9–34.

Spector, P., Stone, J., Cowdery, S.G., Hall, B., Conway, H., Bromley, G., 2017. Rapid early-holocene deglaciation in the ross sea, Antarctica. Geophys. Res. Lett. 44, 7817–7825.

Spencer, C., Yakymchuk, C., Ghaznavi, M., 2017. Visualising data distributions with kernel density estimation and reduced chi-squared statistic. Geoscience Frontiers 8, 1247–1252.

Staiger, J., Gosse, J., Toracinta, R., Oglesby, B., Fastook, J., Johnson, J.V., 2007. Atmospheric scaling of cosmogenic nuclide production: climate effect. J. Geophys. Res.: Solid Earth 112.

Stone, J.O., 2000. Air pressure and cosmogenic isotope production. J. Geophys. Res.: Solid Earth 105, 23753–23759 1978–2012.

Suganuma, Y., Miura, H., Zondervan, A., Okuno, J.i., 2014. East Antarctic deglaciation and the link to global cooling during the Quaternary: evidence from glacial geomorphology and 10Be surface exposure dating of the Sør Rondane Mountains, Dronning Maud Land. Quat. Sci. Rev. 97, 102–120.

Ullman, D.J., Carlson, A.E., Hostetler, S.W., Clark, P.U., Cuzzone, J., Milne, G.A., Winsor, K., Caffee, M., 2016. Final Laurentide ice-sheet deglaciation and Holocene climate-sea level change. Quat. Sci. Rev. 152, 49–59.

Uppala, S.M., Kållberg, P., Simmons, A., Andrae, U., Bechtold, V.d., Fiorino, M., Gibson, J., Haseler, J., Hernandez, A., Kelly, G., 2005. The ERA-40 re-analysis. Q. J. R. Meteorol. Soc. 131, 2961–3012.

Wendt, I., Carl, C., 1991. The statistical distribution of the mean squared weighted deviation. Chem. Geol. Isot. Geosci. 86, 275–285.

Whitehouse, P.L., 2018. Glacial isostatic adjustment modelling: historical perspectives,

recent advances, and future directions. Earth Surface Dynamics 6, 401–429.

Young, N.E., Schaefer, J.M., Briner, J.P., Goehring, B.M., 2013. A 10Be production-rate calibration for the Arctic. J. Quat. Sci. 28, 515–526.

Ziegler, L.B., Constable, C.G., Johnson, C.L., Tauxe, L., 2011. PADM2M: a penalized maximum likelihood model of the 0-2 Ma palaeomagnetic axial dipole moment. Geophys. J. Int. 184, 1069–1089.

Zweck, C., Zreda, M., Desilets, D., 2013. Snow shielding factors for cosmogenic nuclide dating inferred from Monte Carlo neutron transport simulations. Earth Planet. Sci. Lett. 379, 64–71.